RESEARCH ARTICLE





Solid-state NMR for the analysis of interface excesses in Li-doped MgAl₂O₄ nanocrystals

André A. Bernardes¹ | Andre L. da Silva¹ | Jefferson Bettini² | Jair C. C. Freitas³ | Ricardo H. R. Castro⁴ | Douglas Gouvêa¹ |

²Brazilian Nanotechnology National Laboratory (LNNano), Rua Giuseppe Maximo Scolfaro, Campinas, São Paulo, Brazil

³Laboratory of Carbon and Ceramic Materials, Department of Physics, Federal University of Espírito Santo (UFES), Vitória, Espírito Santo, Brazil

⁴Department of Materials Science and Engineering, Lehigh University, Bethlehem, Pennsylvania, USA

Correspondence

Andre L. da Silva, Department of Metallurgical and Materials Engineering, Polytechnic School – University of São Paulo, São Paulo 05508-030, Brazil. Email: andresilva.urussanga@gmail.com

Funding information

RCGI—Research Centre for Greenhouse Gas Innovation; University of São Paulo (USP); FAPESP—São Paulo Research Foundation, Grant/Award Numbers: 2014/50279-4, 2020/15230-5; Brazilian National Oil, Natural Gas and Biofuels Agency; LNNano—Brazilian Nanotechnology National Laboratory, Grant/Award Number: 21831; DMR Ceramics, Grant/Award Number: DMR 2015650; FAPES, Grant/Award Numbers: 280/2021, TO 495/2021

Abstract

Interface segregation plays a governing role in nanocrystalline ceramics properties due to the relative increase in the interfacial volume fraction. However, due to the complexity of the detection and quantification of interfacial excesses at the nanoscale, the role of ionic dopants or additives on microstructural evolution and thermodynamics can be easily underestimated. In this work, we address the spatial distribution of Li⁺ as a dopant in magnesium aluminate spinel nanoparticles. This is achieved through a novel method for the detection and quantification of Li⁺ across the surface, grain boundary, and bulk (crystal lattice). Based on selective lixiviation combined with chemical analysis, we were able to quantify the amount of Li⁺ forming surface excess, whereas the quantitative solid-state nuclear magnetic resonance technique enabled the quantification of Li⁺ segregated in the grain boundaries and dissolved in the lattice. This comprehensive understanding of the Li⁺ distribution across the nanoparticles makes possible an unprecedented interpretation of coarsening and sintering, with a clear correlation between the microstructure and the Li⁺ distribution. Although the work focuses on MgAl₂O₄, the proposed combination of techniques is expected to have a positive impact on the understanding of other multicomponent nanoscale systems.

KEYWORDS

interface segregation, MgAl₂O₄, NMR, sintering, spinel

1 | INTRODUCTION

Dopants, or additives, are commonly used to control the properties and processing of nanoscale oxide-based materials. Improvements in photocatalysis, 1,2 mechanical

strength,³ scintillation,⁴ or phenomena such as sintering and coalescence,^{5,6} are examples of the potential benefits brought by the intentional introduction of foreign ions into a system. Depending on many factors, those dopants can either dissolve to form a solid solution within the crystal

¹Department of Metallurgical and Materials Engineering, Polytechnic School – University of São Paulo, São Paulo, Brazil

journal

lattice (bulk), segregate at existing interfaces, such as the surface and grain boundary (GB), or nucleate a second phase. The dissolution in the lattice is the most accepted pathway taken by dopants and is predicted by phase diagrams; however, particularly at the nanoscale, the dopant distribution cannot be solely determined by the bulk solubility but by a complex energy balance among the surface, the GB, and the bulk. This balance of energy is primarily related to the impact of dopants on each local energetics, affecting the overall thermodynamic metastability as previously described in the literature. 6-14 Thus, one can expect a decrease in the surface and GB energies associated with dopant segregation, which decreases the grain growth rate. The saturation of these interfaces limits the lowering of the GB and surface energies. Thus, with a further increase in dopant concentration, the nucleation of a second phase with its crystalline structure is expected, and the interface energies should not change from this point forward. 15

Note that although the term segregation, or surface excess, has been used in the literature for some time, the fact that these terms have different meanings in different research fields may hinder scientific advancements. According to the IUPAC, segregation is the process that differentiates the composition at an interface or surface from the average or bulk composition. 16 For an interface, the adsorption or surface excess of a given component is defined as "the difference between the amount of component actually present in the system, and that which would be present (in a reference system) if the bulk concentration in the adjoining phases were maintained up to a chosen geometrical dividing surface (Gibbs dividing surface)."17 In the present work, the term segregation or surface excess will be used as a reference to the Gibbs adsorption and segregation. This implies that a single phase exists but with an excess of ions of a certain species accumulated at the interfacial region (this contrasts with metallurgical interpretations of segregation regarding it as the formation of a second phase).

The quantification of the distribution of the dopant across the bulk and interfaces is challenging due to the difficulty of accessing and chemically analyzing each individual interface. Although the total amount of dopants is easily quantified by common techniques, such as X-ray fluorescence spectroscopy (XRF), the spatial distribution relies on extensive electron microscopy analyses associated with spectroscopic tools, such as EDS and EELS.¹⁸ Recently, dopant excess on the surface of nano-oxides has been successfully quantified by a convenient technique called selective lixiviation.^{8,19–21} This technique relies on selectively dissolving the dopant and not the rest of the nanoparticle, using a specific solvent, so that one may quantify how much is located at the surface region. The

technique is robust, showing advantages over other potential techniques, such as XPS, which can be complimentary as XPS is more concerned with the state of dopants on the surface and a proper quantification of the dopant should rely on a series of calibrations.²¹

However, selective lixiviation, or even XPS, does not inform the distribution of the solute between the bulk and GB regions. Although one could attempt to calculate the amount of dopant segregated on grain boundaries by subtracting the surface excess from the total dopant content, the bulk solubility of dopants is usually unknown. Estimations of bulk solubility have been given to specific systems based on the properties of materials, such as distortions in the lattice parameters, 21 or energetic evidence. 20 However, segregated dopants may also impact those physical parameters by directly inducing lattice strain or creating associated defects, highlighting the need for more direct and absolute methods.

This work proposes an analytic strategy to quantify the distribution of dopants across oxide nanoparticles. Specifically, relying on selective lixiviation for surface quantification, we propose the usage of solid-state nuclear magnetic resonance (NMR) to differentiate the chemical environment of the GB and the bulk atoms according to the sites occupied in the material.^{22–25} We apply the methodology to study the total amount of Li₂O and its microstructural distribution (bulk, GBs, and surfaces) using chemical analyses and solid-state ⁷Li NMR. With a comprehensive chemical distribution map, we have performed coarsening experiments of Li-doped MgAl₂O₄ nanopowders to demonstrate how the dopant distribution (solute content in the bulk, evaporation, and segregation in the GBs and/or on the surface) is intimately correlated with the microstructure evolution and shows a significant temperature and grain size dependence. The nanoparticles with segregated Li⁺ were later processed by spark plasma sintering (SPS) to produce a highly dense MgAl₂O₄ nanoceramic aided by the presence of Li⁺ at the interfaces.

2 **MATERIALS AND METHODS**

2.1 Spinel synthesis

Magnesium aluminate spinel was synthesized by simultaneous precipitation in an alcohol solution containing 0.5 M magnesium nitrate hydrate alcoholic solution, Mg(NO₃)₂·6H₂O (Vetec, 98.0%–102.0%), and 0.5 M aluminum nitrate hydrate alcoholic solution, Al(NO₃)₃·9H₂O (Synth. 98.0%-102.0%) in stoichiometric proportion. The precipitation pH of the solution was controlled by an alcoholic solution of 3 M ammonium hydroxide and monitored

TABLE 1 Sample labels according to composition and sintering time.

Sintering time (min)						
Composition (mol% Li)	00	15	30	60	120	240
1.00	10-000	10-015	10-030	10-060	10-120	10-240
2.50	25-000	25-015	25-030	25-060	25-120	25-240

by a digital pH meter analyzer 300 M equipped with an alcoholic electrode model 2A51. The Li⁺ doping (0.00–2.50 mol%) was introduced by a cationic solution of 0.5 M lithium chloride alcoholic solution—LiCl (Synth, 98.0%).

The cationic solution was added simultaneously with the ammonium hydroxide solution to maintain the mixture pH at 10.3 and to simultaneously precipitate the magnesium hydroxide and aluminum hydroxide. This process produced a white suspension, which was centrifuged at 3000 rpm for 6 min, washed in ethyl alcohol (Synth, 99.5%), and centrifuged a second time at 3000 rpm for 6 min. Then, the precipitate was dried at 100°C for 24 h and calcined at 800°C for 5 h with a heating rate of 5°C/min and naturally cooled down inside the furnace to room temperature.

2.2 | Magnesium aluminate pressing and sintering

The powders were uniaxially compressed in a Carver hydraulic press under 100 MPa pressure for 30 s to form cylindrical pellets of 0.4 g with 11.35 mm diameter and 2.50 mm thickness. A total of 36 pellets were compressed (12 samples in triplicate) and weighed. Their geometric densities were calculated by measuring the geometries and masses of the pellets before and after sintering.

The samples were sintered in a Lindberg/Blue M tubular furnace at 1200°C for 15, 30, 60, 120, and 240 min and then labeled according to their composition and sintering time as shown in Table 1. The pellets were inserted and removed from the furnace at 1200°C and cooled to room temperature in air.

2.3 | Spark plasma sintering

 ${
m MgAl_2O_4}$ with a 2.50 mol% lithium content was also processed by SPS. SPS was carried out by the deformable punch SPS (DP-SPS) process, 26 which allows sintering to occur under uniaxial pressure up to 2 GPa at relatively low temperatures. This system also limits grain growth due to the plastic deformation of the pistons and the slippage of grains at the interface between the grains and the piston. 26

In this work, a temperature of 1100°C and a pressure of 200 MPa were applied during the sintering process.

The powder was dried at 400°C under vacuum to eliminate the moisture adsorbed on the surface. The matrix/powder/pistons system was assembled inside a glove box in an argon atmosphere to avoid contact with humidity. The sintering routine consisted of heating from room temperature to 950°C in 7 min, heating from 950 to 1100°C in 3 min, and maintaining the temperature at 1100°C for 5 min with a total sintering time of 15 min. The cooling to room temperature was performed naturally inside the equipment. The pressure of 200 MPa started at 950°C and was maintained until the beginning of the cooling process, that is, until the end of the 15-min sintering cycle.

2.4 | Structural characterization

The X-ray diffractograms of calcined samples were obtained using an X'Pert PRO PW 3040/00 Philips diffractometer equipped with Cu K α radiation at 45 kV and 40 mA. The angular step size was set at $0.02^{\circ}~2\theta$ with a total time of 45 min. The diffractograms were employed to identify the phases present in the material, and the Rietveld method using the whole XRD spectrum was applied to calculate the average crystallite size of the samples. The Malvern PANalytical X'Pert HighScore Plus software and a magnesium aluminate standard obtained under the same conditions as the samples were used for the Rietveld method calculation.

The pycnometric density, $\rho_{\rm He}$, was determined using a Micromeritics AccuPyc II 1340 He gas pycnometer after 200 purges for degassing. The samples were dried at 100°C for 24 h before the analysis.

The specific surface area (SSA) was obtained by N_2 adsorption at 77 K based on the Brunauer–Emmett–Teller method. The analyses were performed using the Micromeritics Gemini III 2375 instrument after pretreating the samples at 400°C under 100 mmHg pressure to remove any moisture adsorbed on the surface.

Equation (1) was used to calculate the total specific area (TSA) of the samples considering a tetrakaidekahedral geometry, where D is the grain size, and ρ_{He} is the pycnometric density. The specific GB area (GBA) of calcined and sintered MgAl₂O₄ was obtained using Equation (2):

$$TSA = \frac{7.1}{\rho_{\text{He}}D} \tag{1}$$

$$GBA = \frac{(TSA - SSA)}{2} \tag{2}$$

journal

Diffuse reflectance infrared Fourier transform spectroscopy was performed using the Thermo-Nicolet Magna 560 spectrometer with a scanning capacity of 400-4000 cm⁻¹ and a resolution of 4 cm⁻¹ to determine the chemical species adsorbed on the surfaces of calcined MgAl₂O₄ nanopowders.

The grain sizes of the sintered pellets were measured using scanning electron microscopy (SEM) images (FEI Inspect F50 FEG microscope). The samples were broken into pieces, and the fractured surfaces were coated with 10 nm gold layers using a Balzers SCS 050 Sputter Coater. The SEM analysis was performed on fractured surfaces using secondary electrons, and the ImageJ software was used to measure the average grain sizes. The results were expressed as the average of at least 100 grains from each sample. The SEM images and respective histograms showing the grain size distribution are exhibited in the Supporting Information section.

Transmission electron microscopy (TEM) images were obtained for a selected sample sintered by SPS. Sample preparation was carried out by reducing the thickness of the pellet by mechanical abrasion, using a Gatan model 601 ultrasonic cutter and ion beam PIPS II. Bright-field scanning TEM was used to obtain the images. The grain size distribution and pore volume fraction were measured using the Gatan Digital micrograph software. For image processing, square geometries were assumed for both grains and pores due to the low circularity and high aspect ratio.

2.5 Solid-state NMR

Solid-state NMR spectroscopy was used to probe the chemical environments of ⁷Li nuclei in the prepared MgAl₂O₄. The NMR spectra were obtained from the 10-000 and 10-000 lixiviated powder samples, 10-060 and 10-240, which were sintered samples, and from 25-010 SPS samples. The sintered and SPS samples were crushed into powder before NMR measurement. As lithium can occupy three different regions in the nanoparticles' structure (e.g., surface, GB, and bulk), and considering that each region presents a different atomic organization, the NMR signals are expected to exhibit different frequency shifts depending on the atomic nucleus environment. Calcined samples with 1.00 mol% Li were selected for the NMR experiments. One of them was lixiviated to wash off the lithium segregated on the surface to compare with a second sample, with lithium distributed in the three regions. A Variant-Agilent 400 MHz spectrometer with a magnetic field of 9.4 T and a frequency of 155.3 MHz for ⁷Li was used. The powders were packed into 4 mm diameter rotors for magic-angle spinning (MAS) experiments conducted at the spinning

rate of 10 kHz. The ⁷Li NMR signals were recorded using single-pulse excitation, with $\pi/2$ pulses of 1.5 μ s duration, a recycle delay of 1000 s, and the accumulation of four scans. The spectra were obtained after the Fourier transform of the free induction decays and were deconvoluted into components with Lorentzian line shapes. The frequency shifts in the ⁷Li NMR spectra, expressed in parts per million (ppm), were measured relative to an aqueous LiCl solution (concentration of 9.7 mol/L).

2.6 Chemical analyses

The chemical compositions of calcined and sintered MgAl₂O₄ were obtained via inductively coupled plasma atomic emission optical spectroscopy (ICP OES). The samples were dissolved by the multi-acid digestion method. The lithium and magnesium contents segregated on the surface were determined by the selective lixiviation method.^{9,18,2,27} Approximately 100 mg of powder was ultrasonicated with 2.0 g of distilled water for 1 h and centrifuged at 13 000 RPM (18 000g-force) for 1 h. The supernatant was collected and diluted in 9.0 g of distilled water and analyzed by ICP OES using a Horiba Jobin Yvon Ultima 2 spectrometer. The residual Cl⁻ from LiCl was measured by XRF using a Malvern Panalytical Zetium spectrometer.

3 RESULTS AND DISCUSSIONS

The chemical analyses of the MgAl₂O₄ nanoparticles containing 1% and 2.5% of Li (10-000 and 25-000) are presented in Table 2.

The powders prepared by chemical precipitation and calcined at 800°C presented a nonstoichiometric MgAl₂O₄ with an Al_2O_3/MgO molar ratio = 1.12, showing an excess of Al₂O₃ but providing satisfactory samples with different Li contents. As LiCl was used to synthesize the nanopowders, Cl was also measured by XRF. The results show 0.2 mol% Cl for both samples. Considering that the values are the same for both samples, we assumed a negligible effect when comparing 10-000 and 25-000 samples.

3.1 | Microstructural evolution during sintering

The densities of the MgAl₂O₄ pellets before and after fastfiring (i.e., rapid introduction of the sample in the furnace) at 1200°C in the tubular furnace at different times are presented in Figure 1. Sintering time "zero" corresponds to the density of the powder compact before fast-firing.

TABLE 2 Chemical analyses of 10-000 and 25-000 MgAl₂O₄ nanopowders.

MgAl ₂ O ₄ sample	Li target concentration (mol%)	Li-measured concentration (mol%)	Al ₂ O ₃ /MgO molar ratio	Cl (mol%)
10-000	1.00	1.43 ± 0.01	1.12 ± 0.01	0.20
25-000	2.50	2.86 ± 0.01	1.12 ± 0.01	0.20

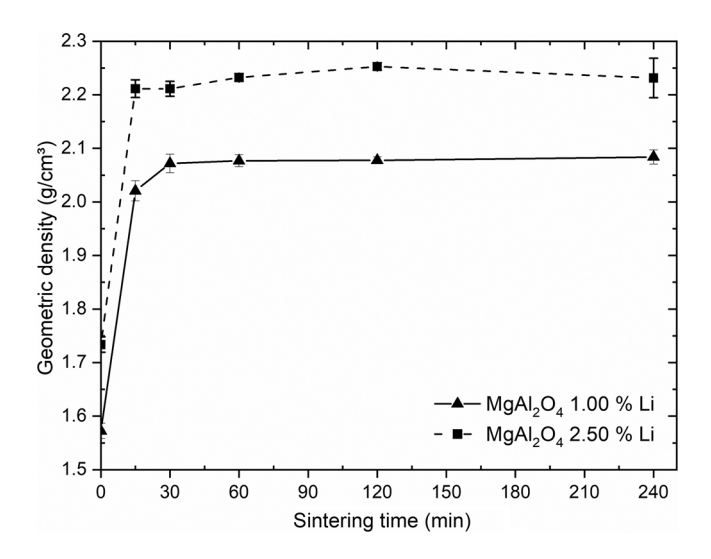


FIGURE 1 Evolution of geometric density for \triangle 1.00 and \blacksquare 2.50 mol% Li MgAl₂O₄ samples sintered at 1200°C.

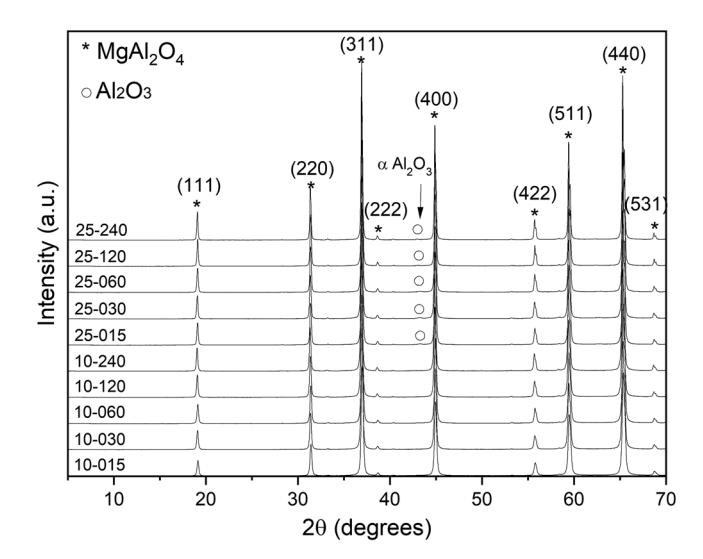


FIGURE 2 XRD patterns of 1.00 and 2.50 mol% Li-doped MgAl $_2$ O $_4$ -sintered samples at different sintering times (K-beta radiation was detected because of the high intensities of the K-alpha radiation peaks).

Fast densification was verified for both Li⁺ concentrations for times up to 30 min but leveling thereafter.²⁸

Figure 2 shows the X-ray diffraction patterns of the coarsened samples. All the samples showed well-defined magnesium aluminate peaks, identified with an asterisk. The peak detected at 43.4° was attributed to a small

amount of alumina (ICDD file 71-1683) precipitated during the sintering of 2.50 mol% Li samples. For 1.00 mol% Li samples, alumina was not detected despite showing the same Al-excess content.

Table 3 summarizes the results of average grain size, pycnometric density (ρ_{He}), SSA, calculated specific GBA, and GBA/SSA ratio for the samples coarsened at the different sintering times. Significant grain growth is observed from 0 to 15 min, for the 10-000 sample, the grain size increased from 4.7 to 70.4 nm (15 times), and for the 25-000 sample from 4.7 to 81.6 nm (17 times). The kinetics of grain growth decreases significantly after 15 min as well as the densification (Figure 1).

For 1.00 mol% Li samples, the GB areas are around twice the surface areas, but a slight reduction is observed from 15 to 60 min sintering times. For 2.50 mol% ${\rm Li}^+$ samples, the GB areas are $\sim\!4$ times the surface areas. Nevertheless, the GBA/SSA ratio increases in the early sintering times, with the highest value occurring at 30 min. After that, the GBA/SSA ratio decreases, indicating a desintering process between 30 and 60 min.

The specific pore volume (SPV) was calculated considering the geometric (ρ_g) and pycnometric (ρ_{He}) densities as represented in the following equation:

$$SPV = \frac{1}{\rho_g} - \frac{1}{\rho_{He}} \tag{3}$$

The evolution of the SPV during sintering is shown in Figure 3.

For both compositions, three regimes are observed with the increase in sintering time: (i) from 0 to 15 min, a pore volume reduction; (ii) from 15 to 60 min, an increase in specific porosity; and (iii) from 60 min on, an almost constant pore volume. The increase in SPV between 15 and 60 min and the decrease in GBA/SSA ratio between 30 and 60 min are the two pieces of evidence that suggest that desintering is occurring at this time range.

The Li content as a function of the sintering time is presented in Figure 4. Li_2O loss by evaporation is observed for both compositions and is more intense in the initial stages of sintering (0–60 min). However, a tendency toward residual Li after a long sintering time is observed, as the 2.50 and 1.00 mol% Li curves tend to converge at 240 min. The Li evaporation seems to be related to the desintering observed between 15 and 60 min; however, a deeper

iournal

TABLE 3 Main physical and microstructural properties of the green bodies and sintered samples.

Samples	Grain size (nm)	Pycnometric density (g/cm³)	SSA (m ² /g)	GBA (m²/g)	GBA/SSA ratio
10-000	4.7 ± 0.3	3.05 ± 0.01	87.8 ± 0.1	204.0 ± 13.0	2.3 ± 0.1
10-015	53.0 ± 0.8	3.52 ± 0.02	6.0 ± 0.1	16.0 ± 0.4	2.7 ± 0.1
10-030	58.0 ± 0.5	3.98 ± 0.02	5.7 ± 0.1	12.5 ± 0.2	2.2 ± 0.1
10-060	63.7 ± 0.8	4.01 ± 0.04	5.4 ± 0.1	11.2 ± 0.3	2.1 ± 0.1
10-120	68.7 ± 1.1	4.21 ± 0.01	4.4 ± 0.1	10.1 ± 0.2	2.3 ± 0.1
10-240	82.2 ± 3.0	4.17 ± 0.03	4.3 ± 0.1	8.2 ± 0.4	1.9 ± 0.1
25-000	4.7 ± 0.3	3.21 ± 0.01	90.7 ± 0.1	189.8 ± 11.8	2.1 ± 0.1
25-015	81.6 ± 3.1	3.48 ± 0.02	2.7 ± 0.1	11.1 ± 0.5	4.1 ± 0.2
25-030	83.6 ± 1.1	3.50 ± 0.01	2.4 ± 0.1	10.9 ± 0.2	4.6 ± 0.2
25-060	104.7 ± 3.5	4.14 ± 0.01	1.9 ± 0.1	7.2 ± 0.3	3.8 ± 0.2
25-120	125.7 ± 1.5	4.15 ± 0.01	1.7 ± 0.1	6.0 ± 0.1	3.6 ± 0.2
25-240	153.3 ± 4.9	4.18 ± 0.03	1.5 ± 0.1	4.8 ± 0.2	3.2 ± 0.2

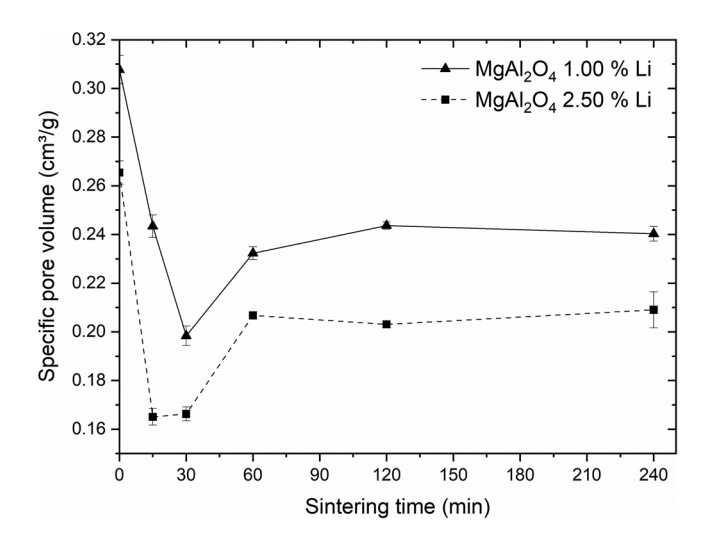


FIGURE 3 Specific pore volume as a function of sintering time for MgAl₂O₄ samples containing 1.00 and 2.50 mol% Li.

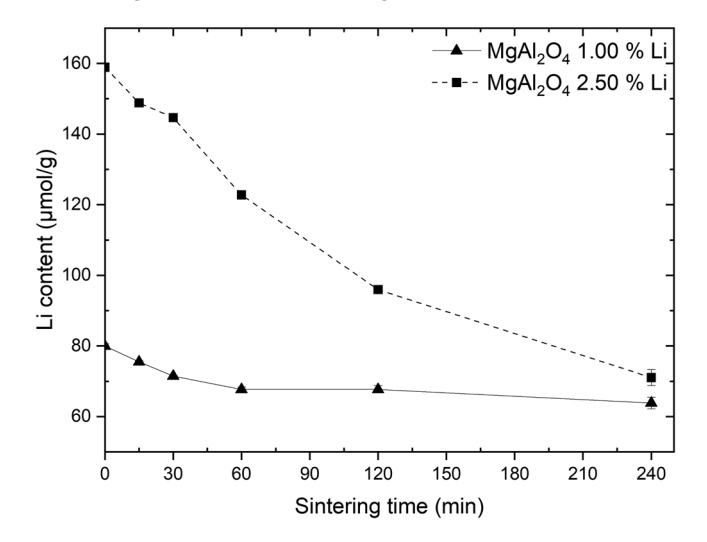


FIGURE 4 Total Li⁺ content of 1.00 and 2.50 mol% Li-sintered MgAl₂O₄ samples at 1200°C.

investigation would be necessary to understand the phenomena deeply.

The distribution of Li⁺ across the system certainly plays an important role in governing the sintering pathways.⁷ This is because, according to the Gibbs adsorption isotherm, the amount of surface and GB excesses should control the local energies. Because sintering is energetically driven by surface elimination and GB formation (and elimination thereafter), the balance of energy between these two interfaces is key for interpreting the microstructural evolution. The observed dynamics in the behaviors suggest that the interfacial chemistries, and hence their respective energies, are equally dynamic during the coarsening, and a detailed analysis of the Li distribution is required for full interpretation of the process.

3.1.1 | Surface composition

Figures 5 and 6 exhibit the Li⁺ and Mg²⁺ surface excesses ($\Gamma_{\rm Li}$ and $\Gamma_{\rm Mg}$) for 1.00 and 2.50 mol% Li-doped MgAl₂O₄-sintered samples, respectively. The results were acquired by chemical analysis of the leaching supernatant obtained by the selective lixiviation method.^{20,7,21} Γ_{Li} increased significantly from 0 to 15 min of sintering for both samples, which was due to grain growth and the consequent reduction in SSA (Table 3). Γ_{Mg} was very low, and no Al³⁺ was detected, demonstrating that MgAl₂O₄ is not soluble in water in the conditions used for the selective lixiviation. For sintering times greater than 15 min, $\Gamma_{\rm Li}$ decreased continually with sintering time as a consequence of Li₂O evaporation, which increased the $\Gamma_{\rm Mg}$ as a result of the MgAl₂O₄ surface exposure.

The Li₂O evaporation was facilitated because part of the total lithium oxide was segregated on the surface of

15512916, 2024, 2, Downloaded from https:

prary.wiley.com/doi/10.1111/jace.19496 by Lehigh University, Wiley Online Library on [24/06/2024]. See the Terms and Conditions (https:

conditions) on Wiley Online Library for rules of use; OA articles are governed by the applicable Creative Commons License

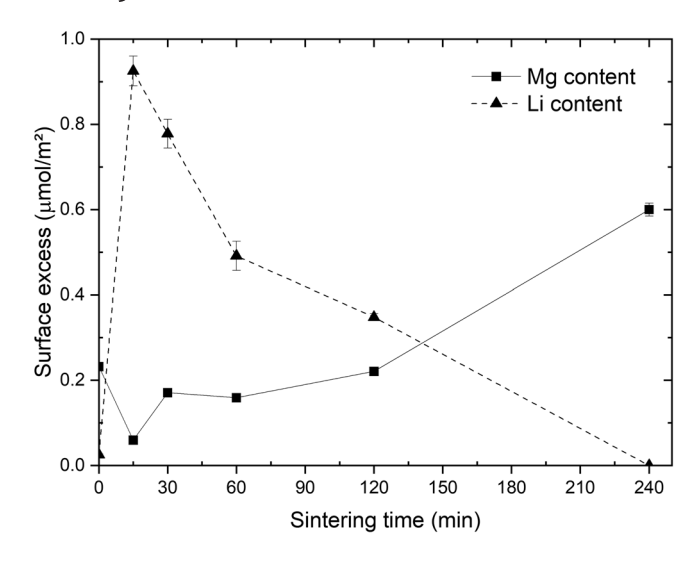


FIGURE 5 Surface excess of Li⁺ and Mg^{2+} for 1.00 mol% Li⁺-sintered $MgAl_2O_4$ samples.

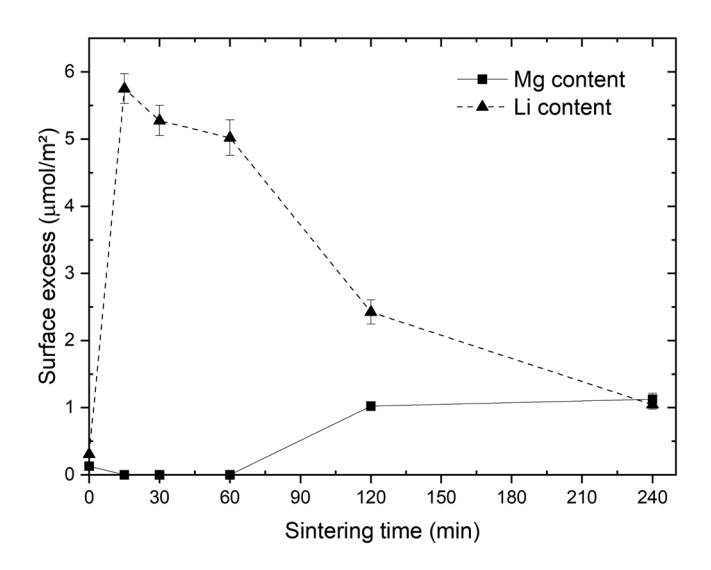


FIGURE 6 Surface excess of Li⁺ and Mg²⁺ for 2.50 mol% Li⁺-sintered MgAl₂O₄ samples.

 $MgAl_2O_4$. However, as presented in Figure 4, after a long sintering time, the Li content tended to stabilize. Thus, to better understand the total residual amount of Li in the $MgAl_2O_4$, the total Li concentration was plotted as a function of surface excess (Figure 7).

Figure 7 shows that the total Li concentration is roughly proportional to the surface excess. By extrapolating the observed trends, a residual amount of about $60 \, \mu \text{mol g}^{-1}$ is obtained for both samples. This residual Li can be related to the solute content in the bulk and to the GB segregation. In both cases, evaporation is hindered by the protection of the refractory MgAl₂O₄ lattice. The GB and surface excess can also be modified by the intense reduction in GBA due to the redistribution of Li⁺ from the GB to the surface during grain growth and the consequent Li₂O evaporation.

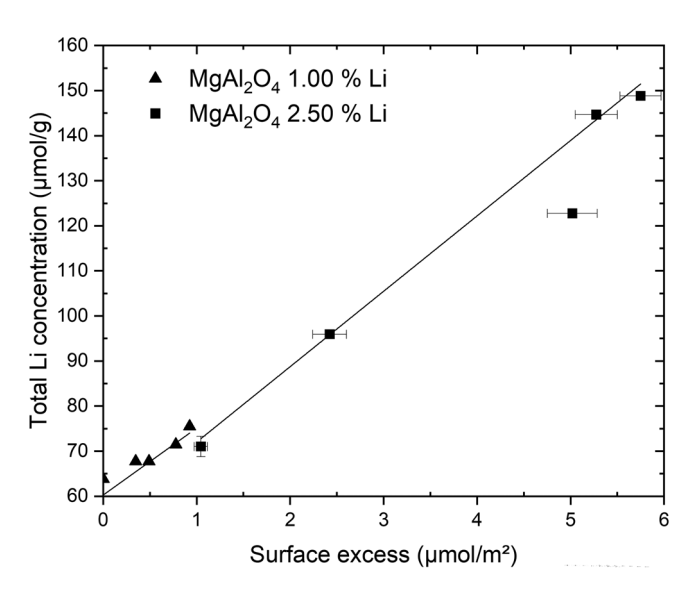


FIGURE 7 Total Li concentration as a function of surface excess of MgAl₂O₄ sintered at 1200°C.

Quantification of surface and GB segregation is fundamentally dependent on bulk solubility. The total amount of Li⁺ is easily determined by sample dissolution and chemical analysis as well as surface segregation by the selective lixiviation method. However, the distinction between the GB and the solute content in the bulk has been very difficult to obtain so far. In this study, the analysis of solid-state ⁷Li NMR spectra is proposed as a tool to separate the GB and bulk contributions, as presented in the next section.

3.2 | Solid-state ⁷Li NMR: grain boundary and surface segregation and solute content in the bulk

The NMR results were used to estimate the lithium distribution on the surface, at the GB, and in the bulk of the calcined and sintered MgAl₂O₄ samples. This approach was possible because the ⁷Li NMR chemical shift depends on the chemical environment of the ⁷Li nuclei. When comparing the ⁷Li NMR spectra obtained for the non-lixiviated sample with the lixiviated one, three different spectral components are expected to be found for the non-lixiviated samples (surface, GB, and bulk contributions), and two components for the lixiviated sample (GB and bulk contributions).

Although the literature suggests that Li⁺ occupies the tetrahedral and octahedral sites of MgAl₂O₄, this section proposes to demonstrate that the Li⁺ dissolved in the bulk occupies only one position: octahedral coordination, replacing Al³⁺ ions.³¹ The relative area of a given NMR signal is proportional to the number of nuclei associated with

15512916, 2024, 2, Downloaded from https://ceramics.onlinelibrary.wiley.com/doi/10.1111/jace.19496 by Lehigh University, Wiley Online Library on [24/06/2024]. See the Terms and Condit and-conditions) on Wiley Online Library for rules of use; OA articles are governed by the applicable Creative Commons License

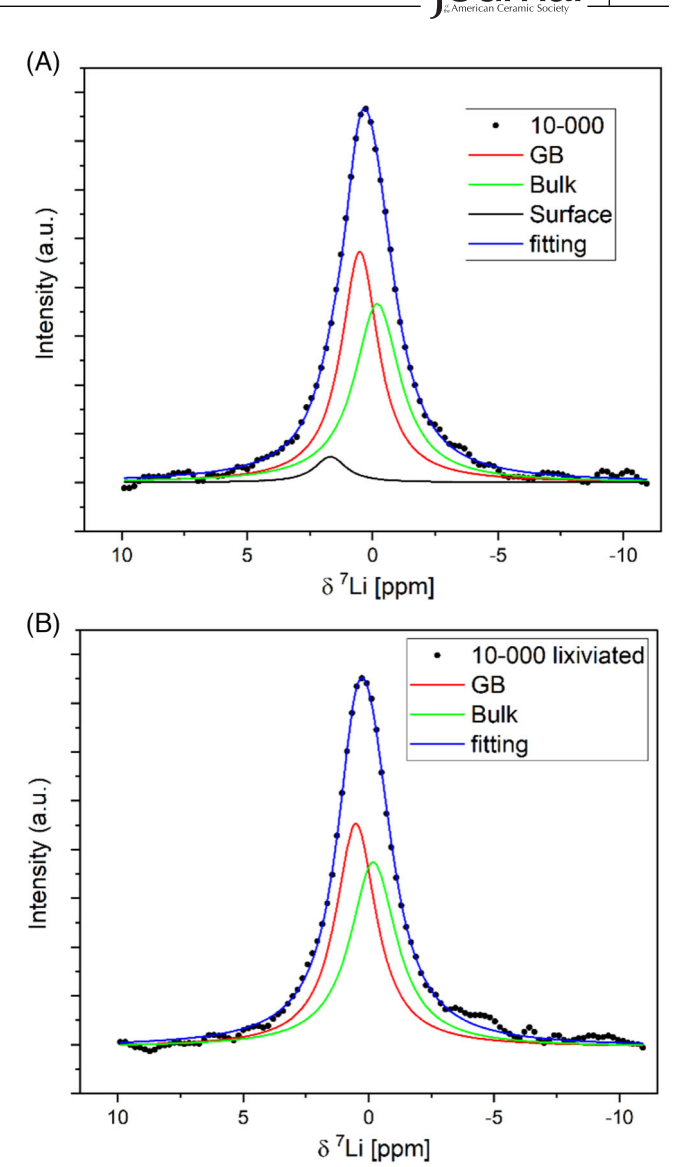
that signal in the sample. Hence, the total area of the cumulative NMR signal is proportional to the total quantity of lithium present in the samples, and the chemical shift is different for each atomic environment: surface, GB, and bulk (octahedral or tetrahedral). Therefore, the deconvolution of the total ⁷Li NMR signal allowed us to quantify the solute content in the bulk and the surface and GB

It is worth stressing that ⁷Li is a quadrupolar nucleus (spin = 3/2), and thus, the ⁷Li MAS NMR spectra are affected by the quadrupole coupling to the electric field gradient (EFG) at the nuclear site, besides the shielding interaction and the homonuclear dipole coupling; more specifically, the frequency shift is determined by the isotropic chemical shift and second-order quadrupoleinduced shifts, whereas the lineshape and the linewidth are due to second-order quadrupole and ⁷Li-⁷Li dipole coupling effects not removed by MAS.32 In the case of the ⁷Li NMR spectra presented here, the first-order quadrupole coupling is mainly responsible for the appearance of a set of spinning sidebands in all detected spectra. In turn, the second-order quadrupole contribution to the signal associated with the central transition (which corresponds to the spectra shown in Figures 8 and 9) is small for ⁷Li nuclei in the materials analyzed, as revealed by the narrow and symmetric lineshape of all detected signals. This is a consequence of the moderate value of the electric quadrupole moment of the ⁷Li nucleus³² and also of the small EFG at the nuclear sites expected in Li₂O, LiAl₅O₈, and other diamagnetic oxygen-containing Li compounds. 33,22

Some studies have demonstrated more than one contribution to the ⁷Li NMR spectra for oxides with only one octahedral site. For instance, Luca et al. suggested the existence of two contributions for ⁷Li NMR in a similar site, but one uncoupled and another weakly coupled to the conduction band of TiO2.34,35

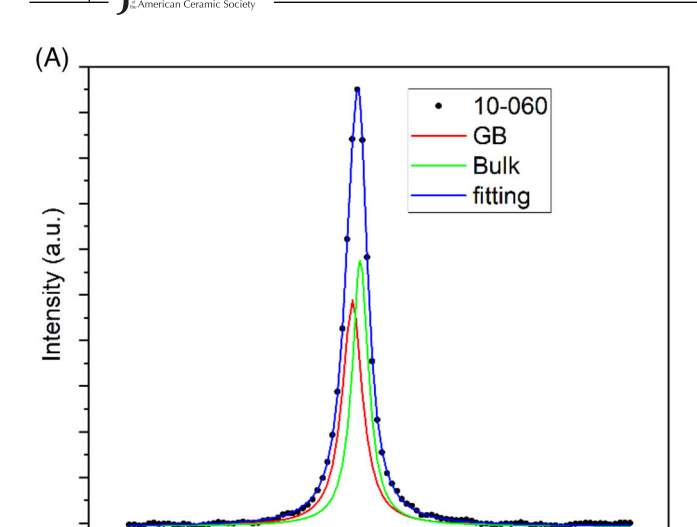
The different contributions of surface and bulk atoms for the NMR spectrum have been demonstrated for metallic nanoparticles. The field sweep Fourier transform method has been used to separate the contributions of subsurface layers of Pt nanoparticles in the ¹⁹⁵Pt NMR spectrum. Signal deconvolution shows that each sublayer has its contribution to the total spectrum, whereas the outermost ones have wider peaks with different chemical shifts.²⁵ In this study, a similar approach was used to identify the contribution of ⁷Li nuclei to the NMR spectra, considering their location in the nanostructure of MgAl₂O₄ samples.

The comparison of deconvoluted ⁷Li NMR spectra of non-lixiviated and lixiviated MgAl₂O₄ nanopowders allowed identifying the signals related to the lithium segregated on the surface, at the GB, and dissolved in the bulk (Figure 8). These signals were identified by recording



⁷Li magic-angle spinning nuclear magnetic resonance (NMR) spectra obtained for the 10-000 (A) and 10-000 lixiviated (B) samples. The dots correspond to the experimental data, the blue line is the fitted spectrum, and the other lines indicate the components obtained by spectral deconvolution.

the NMR spectra before and after lixiviation, that is, first, a non-lixiviated sample (10-000) was analyzed, then the lithium from the surface was removed by selective lixiviation and a new NMR experiment was carried out. After lixiviation, only two contributions assigned to the GB and solute content in the bulk were seen instead of the three contributions found for non-lixiviated samples. In addition to finding the signals related to lithium excess on the surface and GBs, and dissolved in the bulk, the NMR results also show that the superficial lithium was successfully removed from the surface by selective lixiviation. The total lithium concentration was obtained from the chemical composition results from the ICP analysis



-5

-10

iournal

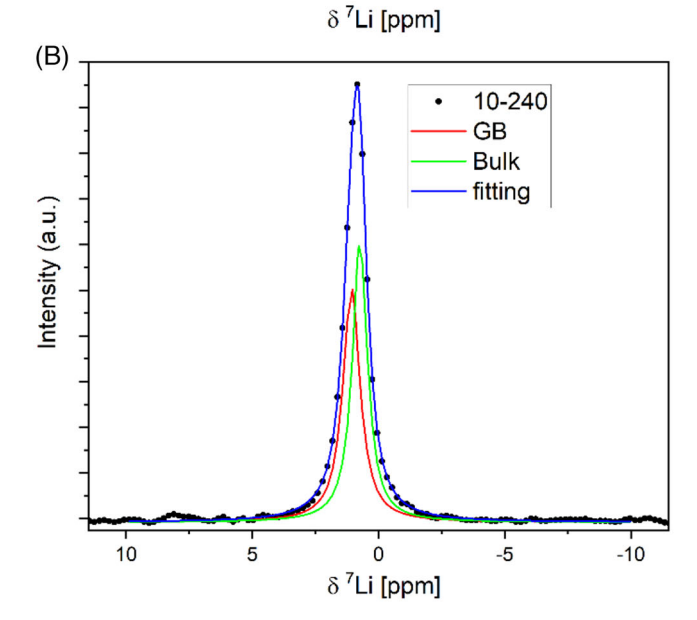


FIGURE 9 ⁷Li magic-angle spinning nuclear magnetic resonance (NMR) spectra obtained for 10-060 (A) and 10-240 (B) sintered samples. The dots correspond to the experimental data. The blue line is the fitted spectrum, and the other lines indicate the components obtained by spectral deconvolution.

of dissolved $MgAl_2O_4$ nanopowder, and the proportion of each signal was obtained by the integration of the deconvolved NMR peaks (Table 4).

The signature of each signal concerning the chemical shift was considered a function of the magnetic shielding. Thus, chemical shifts closer to zero or negative values were assigned to Li⁺ content dissolved in the bulk. The more disordered sites were considered to have less shielding and therefore led to more positive shifts compared to the bulk. As the structure of the grain boundaries is intermediate between the bulk and surface sites, the signals due to ⁷Li nuclei in atoms segregated on the surface are assumed to have a more positive shift than those segregated at the GB.

TABLE 4 Chemical shifts and relative intensities obtained from the deconvolution of the ⁷Li nuclear magnetic resonance (NMR) spectra of samples treated at different sintering times.

		Relative	Chemical
Sample	Peak	intensity	shift
10-000	Bulk	47 ± 3	-0.19 ± 0.06
	GB	49 ± 5	0.51 ± 0.05
	Surface	4 ± 2	1.68 ± 0.07
10-000 lixiviated	Bulk	48 ± 2	-0.19 ± 0.05
	GB	52 ± 2	0.51 ± 0.04
10-060	Bulk	49 ± 1	0.72 ± 0.01
	GB	51 ± 1	1.04 ± 0.02
10-240	Bulk	51 ± 5	0.74 ± 0.01
	GB	49 ± 6	1.07 ± 0.02
25-010 SPS	Bulk	33 ± 2	0.54 ± 0.06
	GB	43 ± 3	0.86 ± 0.01
	Surface	24 ± 2	1.06 ± 0.01

Abbreviation: SPS, spark plasma sintering.

Therefore, for nano MgAl₂O₄, the octahedral coordinated Li⁺ can be supposed to be associated with the solute content in the bulk and the tetrahedral to be associated with the GB.

The chemical shift above 0 ppm is generally assigned to the tetrahedrally coordinated Li⁺ and below 0 ppm to the octahedrally coordinated Li⁺ for silicates.²² However, LiAl₅O₈ presents a positive chemical shift of approximately 0.3 ppm in which Li⁺ is exclusively octahedrally coordinated.36-38 Nevertheless, six- and fourfold coordinated sites have been ascribed to Li-doped MgAl₂O₄ with the lowest chemical shift attributed to octahedral sites and the highest to tetrahedral sites.²² Similarly, in the interpretation presented in this work, the contributions of lithium dissolved in the bulk and segregated in the GB are assigned to the lower and higher chemical shifts, respectively. Also note that all of the detected signals show a displacement toward higher chemical shifts and a progressive narrowing with increasing sintering time, indicating a progressive improvement in the structural ordering around the Li sites.

Three contributions from the deconvolution of the NMR spectra were found for the 10-000 sample before lixiviation, which represents the bulk, GB, and surface contributions (Figure 8 and Table 4). After lixiviating the lithium from the surface, only two contributions were identified (Figure 8 and Table 4), which are ascribed to the bulk and the GB. The ratios of the deconvoluted areas of the bulk, GB, and surface components before and after lixiviation were 47:49:4 and 48:52:0, respectively, representing the ⁷Li distribution in each of these regions (Table 4). It is worth noting that the amount of Li⁺ segregated in the MgAl₂O₄ nanopowders was close to the results obtained previously.

Iournal

Total residual lithium, solute content in the bulk and in the grain boundaries (GBs) derived from the ⁷Li nuclear magnetic resonance (NMR) results, and GB excess, calculated by multiplying the solute content in the GB by the GB area (GBA).

Samples	Total Li ⁺ [μmol/g]	Solute content in the bulk [μ mol/g]	Solute content in the GB [μ mol/g]	GB excess [µmol/m²]
10-000	80.0 ± 0.6	37.2 ± 1.1	39.2 ± 2.3	0.2 ± 0.1
10-000 lixiviated	77.7 ± 0.6	37.1 ± 1.3	40.6 ± 2.4	0.2 ± 0.1
10-060	67.7 ± 0.6	33.0 ± 11.6	34.7 ± 5.7	3.0 ± 0.7
10-240	63.8 ± 1.6	32.7 ± 10.0	31.1 ± 5.5	3.8 ± 0.7
25-010 SPS	158.9 ± 0.2	52.4 ± 13.2	68.3 ± 8.3	1.5 ± 0.4

Abbreviation: SPS, spark plasma sintering.

Blaakmeer et al. also identified three contributions in solid-state 7Li NMR spectra of MgAl₂O₄ samples using ²⁷Al-⁷Li rotational echo double resonance (REDOR) experiments: two contributions associated with immobile Li⁺ ions (in tetrahedral and octahedral sites) and a lowintensity signal (only visible in REDOR spectra recorded with long dephasing times or in single-pulse excitation spectra recorded with short recycle delays) due to mobile Li+ ions in an octahedral site (exhibiting faster spinlattice relaxation).²² As the surface-segregated Li⁺ ions are expected to have higher mobility than that dissolved in the bulk or segregated in the GB, this weak signal can be associated with the surface contribution identified in the present study. Similarly, the results reported by Blaakmeer et al. showed that the intensity of the surface contribution in the ⁷Li NMR spectrum is only 5% of the total concentration (Table 4). Note that the chemical shifts in the present study are $\delta = 1.68$ or 1.06 ppm for different samples, whereas the shift obtained by Blaakmeer 22 is $\delta = -0.25$ ppm. These shift values cannot be compared because of the difference in Al/Mg stoichiometry, although the comparison of the contributions of the signal to the total concentration is still valid.

Figure 9 shows the ⁷Li NMR spectra for 10-060 and 10-240 MgAl₂O₄ sintered samples. Even if some segregated lithium remained on the surface of the 10-060 sample, only two peaks were reliably identified for both samples after deconvolution, which represents the lithium segregated in the GB and dissolved in the bulk. The amount of surface-segregated lithium is below the limit of detection. Consistent with the interpretation presented above for the ⁷Li NMR spectra of the non-sintered powders, the lowest chemical shift was associated with the sixfold coordinated, octahedral site (bulk component), and the highest chemical shift with the fourfold coordinated, tetrahedral site (GB component). The distribution of the amounts of Li⁺ ions corresponding to the bulk and GB components is very similar for the sintered and non-sintered powder samples (see Table 4).

A comparison of the total amount of Li⁺ at different sites during sintering is exhibited in Table 5.

The total Li⁺ content slightly decreased from the nonlixiviated 10-000 sample to the lixiviated 10-000 one, which can be associated with the removal of lithium from the MgAl₂O₄ surface. For 10-060 and 10-240 samples, due to evaporation during sintering, the removal of lithium was even greater. The solute content in the bulk was virtually constant for all samples, but the solute content in the GB decreased as the sintering time increased, which is a consequence of the lithium evaporation and redistribution throughout the sample. These results also lead to the conclusion that part of the total lithium in the GB is redistributed to the surface as the sintering time increases and then evaporates. In contrast, the GB excess increased due to the reduction of GB during grain growth. As the GB excess is related to the interface energy, its increment causes a reduction in the GB energy and consequently leads to an increase in the interface stability, promoting densification.15

The segregation of Al3+ into the GBs of sintered MgAl₂O₄ has been detected, and the studies show that it generates a negative space-charge potential due to Mg vacancies (V''_{Mg}) and a consequent positive subgrain defect probably associated with substitutional aluminum in the Mg positions (Al_{Mg}).^{39–41} Nuns et al.³⁹ proposed that the octahedral vacancies predominate over the tetrahedral, and the GBs have a net negative space-charge potential.³⁹ Their results suggest that the segregation of Li⁺ in GBs for sintered MgAl₂O₄ can be promoted by the negative electrical potential in GBs, which increases the negative charge by substituting lithium in the octahedral aluminum site (Li''_{Al}) and consequently increasing the electrical resistance of the GBs. 42

Modification of the bulk and GB electrical conductivity of Li-doped MgAl₂O₄ is an indication of the dissolution of the solute in the bulk and GB segregation.⁴² Although difficult to quantify, indirect measurements provide strong evidence that GB segregation plays a key role in interface

15512916, 2024, 2, Downloaded from https://ceramics.onlinelibrary.wiley.com/doi/10.1111/jace.19496 by Lehigh University, Wiley Online Library on [24/06/2024]. See the Terms and Conditions (https://onlinelibrary.wiley.com/emrs-and-conditions) on Wiley Online Library or rules of use; OA arctics are governed by the applicable Creative Commons License

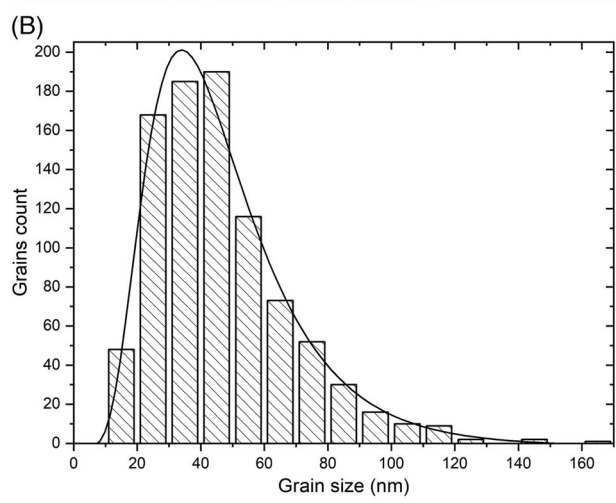


FIGURE 10 Bright-field scanning transmission electron microscopy image showing the nanometric grains of the 25-010 spark plasma sintering (SPS) sample (A), and the grain size distribution presenting a log-normal distribution (B).

engineering and nanoparticle application. If lithium evaporates from the surface, one may expect this vapor to stabilize the pores. In this case, a sintering strategy such as applying external pressure during sintering, aiming to eliminate porosity and reduce the sintering temperature, can be applied. In the same way, to minimize grain growth, SPS is an interesting technique that combines pressure with a high heating rate and low sintering times.^{43,44}

3.3 | Spark plasma sintering

Deformable punch SPS (DP-SPS) was performed on the 25-010 SPS sample under uniaxial pressure at 200 MPa and

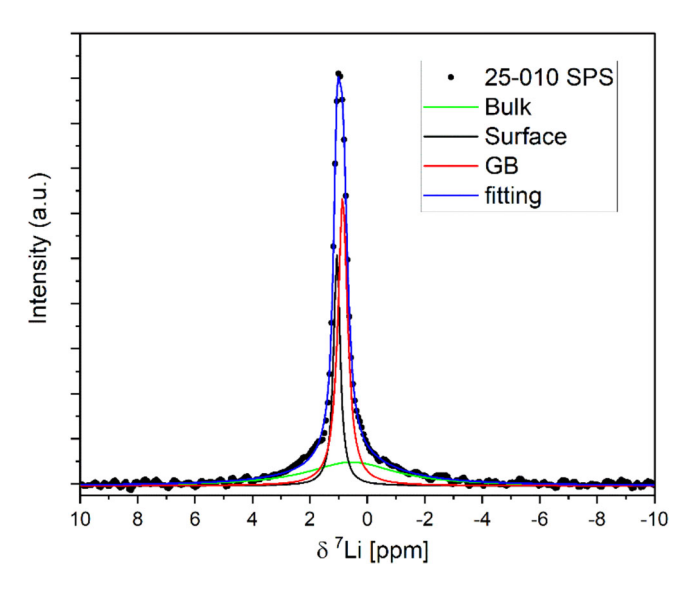


FIGURE 11 ⁷Li magic-angle spinning nuclear magnetic resonance (NMR) spectrum obtained for the 25-010 spark plasma sintering (SPS) sample. The dots correspond to the experimental data, the blue line is the fitted spectrum, and the other lines indicate the components obtained by spectral deconvolution.

 1100°C aiming to retain the lithium dopant in the GBs, stabilizing this interface, and minimizing grain growth. The microstructure of the sample obtained by bright-field SEM is shown in Figure 10A. The sample presented a high density with an average grain size of 46 ± 1 nm (Figure 10B), confirming that SPS of lithium-doped MgAl $_2$ O $_4$ nanopowders allows maintaining the nanometric grains simultaneously to the full densification. The combination of pressure and low sintering temperature promoted complete pore elimination with controlled grain growth, achieving a final grain size 10 times larger than the initial crystallite size. In this sintering condition, Li $_2$ O evaporation can be prevented, and Li ions are expected to dissolve in the bulk and segregate in the GBs.

The lithium distribution in the 25-010 SPS sample was obtained by solid-state ⁷Li NMR (Figure 11 and Tables 4 and 5); in this case, the spectrum obtained was successfully fitted using three spectral components. As the NMR experiment is performed using powders, the 25-010 SPS sample was milled before the analysis. The milling process was surprisingly easy, which suggests that the fracture occurred at the GBs, creating new surfaces (solid-vapor interface), and consequently exposing Li⁺. Therefore, the three contributions in the NMR result were again associated with the GB, bulk, and the new surface. The chemical shifts observed are close to the values corresponding to the sintered MgAl₂O₄; the distribution of Li⁺ in the bulk and GB is presented in Table 5. The solute content in the GB was twice as high in the 25-010 SPS sample as it was in

Journal | 134

sintered samples. However, the GB excess was half of the sintered material (Table 5).

4 | CONCLUSIONS

The paper presents for the first time a comprehensive description of the dynamic positioning of Li as a dopant in MgAl₂O₄ nanoparticles during microstructural evolution. The evolution of both surface and GB chemistries translates into a dynamic driving force for coarsening phenomena, highlighting the challenges that are ubiquitous to other multicomponent oxide systems. The distribution of Li could only be determined by the application of a novel methodology combining selective lixiviation and ⁷Li NMR experiments. The analyses showed that Li⁺ is mainly distributed in the bulk and GB, whereas the surfacesegregated portion evaporates during sintering, leading to a desintering process. Geometric density measurements did not show any significant change after 30 min of sintering, whereas the grain sizes increased, reaching ~82 and ~153 nm at 240 min for samples doped with 1.0 and 2.5 mol% Li⁺, respectively. The Li content as a function of sintering time showed a considerable decrease, associated with Li evaporation, which was more intense in the first stages of sintering (0-60 min). Moreover, the use of NMR to estimate the lithium distribution in the bulk and at the interfaces refers to a novel interpretation of sintering additives. To demonstrate a nanoparticle application, as an alternative to fast-firing technology, the SPS allowed the decrease of the sintering temperature and, consequently, the Li evaporation to obtain a highly dense MgAl₂O₄ nanoceramic. This novel understanding of dopant distribution and its dynamics during coarsening/sintering is critical for understanding multicomponent oxides.

ACKNOWLEDGMENTS

We gratefully acknowledge support from the RCGI—Research Centre for Greenhouse Gas Innovation, hosted by the University of São Paulo (USP) and sponsored by FAPESP—São Paulo Research Foundation (2014/50279-4 and 2020/15230-5) and Shell Brasil, along with the strategic importance of the support given by ANP (Brazilian National Oil, Natural Gas and Biofuels Agency) through the R&D levy regulation. This research was also supported by LNNano—Brazilian Nanotechnology National Laboratory, CNPEM/MCTIC, TEM proposal no. 21831. RHRC thanks DMR Ceramics DMR 2015650. JCCF acknowledges the support from FAPES (TO 280/2021, TO 495/2021). The authors are also grateful to the Laboratory for Research and Development of Methodologies for Crude Oil Analysis (LabPetro), and to the Federal University

of Espírito Santo (UFES), for the use of experimental facilities.

ORCID

André A. Bernardes https://orcid.org/0000-0003-2108-9713

Andre L. da Silva https://orcid.org/0000-0001-8006-8870

Douglas Gouvêa https://orcid.org/0000-0003-3607-8793

REFERENCES

- Da Silva AL, Muche DNF, Dey S, Hotza D, Castro RHR. Photocatalytic Nb₂O₅-doped TiO₂ nanoparticles for glazed ceramic tiles. Ceram Int. 2016;42(4):5113–22. https://doi.org/10.1016/j.ceramint.2015.12.029
- Gandelman H, da Silva AL, Ramos B, Gouvêa D. Interface excess on Sb-doped TiO₂ photocatalysts and its influence on photocatalytic activity. Ceram Int. 2021;47(1):619–25. https://doi.org/10. 1016/j.ceramint.2020.08.169
- Neves DCOS, da Silva AL, de Oliveira Romano RC, Gouvêa D. Fe₂O₃-doped SnO₂ membranes with enhanced mechanical resistance for ultrafiltration application. J Eur Ceram Soc. 2020;40(15):5959–66. https://doi.org/10.1016/j.jeurceramsoc. 2020.06.077
- Wang J, Wang Q, Li H, Shi J, Xiu H, Ren G, et al. Segregation effects of Tl and Li ions on the scintillation properties of NaI:Tl, Li single crystals. J Cryst Growth. 2023;612:127199. https://doi. org/10.1016/j.jcrysgro.2023.127199
- Caliman LB, Muche D, Silva A, Ospina CA, Machado IF, Castro RHR, et al. Effect of segregation on particle size stability and SPS sintering of Li₂O-Doped magnesium aluminate spinel. J Eur Ceram Soc. 2019;39(10):3213–20. https://doi.org/10.1016/j. jeurceramsoc.2019.04.017
- Muche DNF, da Silva AL, Nakajima K, Gouvêa D, Castro RHR. Simultaneous segregation of lanthanum to surfaces and grain boundaries in MgAl₂O₄ nanocrystals. Appl Surf Sci. 2020;529:147145. https://doi.org/10.1016/j.apsusc.2020.147145
- Bernardes AA, Caliman LB, da Silva AL, Bettini J, Guimarães KL, Gouvea D. Li₂O-doped MgAl₂O₄ nanopowders: energetics of interface segregation. J Am Ceram Soc. 2020;103(4):2835–44. https://doi.org/10.1111/jace.16942
- Da Silva AL, Muche DNF, Caliman LB, Bettini J, Castro RHR, Navrotsky A, et al. TiO₂ surface engineering to improve nanostability: the role of interface segregation. J Phys Chem C. 2019;123(8):4949–60. https://doi.org/10.1021/acs.jpcc.8b12160
- Gouvêa D, do Rosário DCC, Caliman LB. Surface and grainboundary excess of ZnO-doped SnO₂ nanopowders by the selective lixiviation method. J Am Ceram Soc. 2017;100(9):4331–40. https://doi.org/10.1111/jace.14973
- Muche DNF, Marple MAT, Sen S, Castro RHR. Grain boundary energy, disordering energy and grain growth kinetics in nanocrystalline MgAl₂O₄ spinel. Acta Mater. 2018;149:302–11. https://doi.org/10.1016/j.actamat.2018.02.052
- Pereira GJ, Bolis K, Muche DNF, Gouvêa D, Castro RHR. Direct measurement of interface energies of magnesium aluminate spinel and a brief sintering analysis. J Eur Ceram Soc. 2017;37(13):4051–58. https://doi.org/10.1016/j.jeurceramsoc. 2017.05.035

- 12. McCune RC, Wynblatt P. Calcium segregation to a magnesium oxide (100) surface. J Am Ceram Soc. 1983;66(2):111–17.
- Nowotny J. Science of ceramic interfaces. New York: Elsevier; 1991
- Castro RHR. Interfacial energies in nanocrystalline complex oxides. Curr Opin Solid State Mater Sci. 2021;25(3):100911. https://doi.org/10.1016/j.cossms.2021.100911
- Castro RHR, Gouvêa D. Sintering and nanostability: the thermodynamic perspective. J Am Ceram Soc. 2016;99(4):1105–21. https://doi.org/10.1111/jace.14176
- 16. Clarke JB, Hastie JW, Kihlborg LHE, Metselaar R, Thackeray MM. Definitions of terms relating to phase transitions of the solid state (IUPAC Recommendations 1994). Pure Appl Chem. 1994;66(3):577–94. https://doi.org/10.1351/pac1994660/3:hyphenbreak \(\lambda/\lambda/3:hyphenbreak)\lambda/3:hyphenbreak)\(\lambda/3:hyphenbreak)\(\lambda/3:hyphenbreak)\(\lambda/3:hyphenbreak)\(\lambda/3:hyphenbreak)\(\lambda/3:hyphenbreak)\(\lambda/3:hyphenbreak)\(\lambda/3:hyphenbreak)\(\lambda/3:hyphenbreak)\(\lambda/3:hyphenbreak)\(\lambda/3:hyphenbreak)\(\lambda/3:hyphenbreak)\(\lambda/3:hyphenbreak)\(\lambda/3:hyphenbreak)\(\lambda/3:hyphenbreak)\(\lambda/3:hyphenbreak)\(\lambda/3:hyphenbreak)\(\lambda/3:hyphenbreak)\(\lambda/3:hyphenbreak)\(\lambda/3:hyphenbreak)\(\lambda/3:hyphenbreak)\(\lambda/3:hyphenbreak)\(\lambda/3:hyphenbreak)\(\lambda/3:hyphenbreak)\(\lambda/3:hyphenbreak)\(\lambda/3:hyphenbreak)\(\lambda/3:hyphenbreak)\(\lambda/3:hyphenbreak)\(\lambda/3:hyphenbreak)\(\lambda/3:hyphenbreak)\(\lambda/3:hyphenbreak)\(\lambda/3:hyphenbreak)\(\lambda/3:hyphenbreak)\(\lambda/3:hyphenbreak)\(\lambda/3:hyphenbreak)\(\lambda/3:hyphenbreak)\(\lambda/3:hyphenbreak)\(\lambda/3:hyphenbreak)\(\lambda/3:hyphenbreak)\(\lambda/3:hyphenbreak)\(\lambda/3:hyphenbreak)\(\lambda/3:hyphenbreak)\(\lambda/3:hyphenbreak)\(\lambda/3:hyphenbreak)\(\lambda/3:hyphenbreak)\(\lambda/3:hyphenbreak)\(\lambda/3:hyphenbreak)\(\lambda/3:hyphenbreak)\(\lambda/3:hyphenbreak)\(\lambda/3:hyphenbreak)\(\lambda/3:hyphenbreak)\(\lambda/3:hyphenbreak)\(\lambda/3:hyphenbreak)\(\lambda/3:hyphenbreak)\(\lambda/3:hyphenbreak)\(\lambda/3:hyphenbreak)\(\lambda/3:hyphenbreak)\(\lambda/3:hyphenbreak)\(\lambda/3:hyphenbreak)\(\lambda/3:hyphenbreak)\(\lambda/3:hyphenbreak)\(\lambda/3:hyphenbreak)\(\lambda/3:hyphenbreak)\(\lambda/3:hyphenbreak)\(\lambda/3:hyphenbreak)\(\lambda/3:hyphenbreak)\(\lambda/3:hyphenbreak)\(\lambda/3:hyphenbreak)\(\lambda/3:hyphenbreak)\(\lambda/3:hyphenbreak)\(\lambda/3:hyphenbreak)\(\lambda/3:hyphenbreak)\(\lambda/3:hyphenbreak)\(\lambda/3:h
- 17. IUPAC. Compendium of chemical terminology, 2nd ed. (the "Gold Book"). Compiled by A. D. McNaught and A. Wilkinson. Blackwell Scientific Publications, Oxford (1997). Online version (2019-) created by S. J. Chalk. ISBN 0-9678550-9-8 . https://doi.org/10.1351/goldbook.s06171
- da Silva AL, Bettini J, Bernardes AA, Castro RHR, Gouvêa D. Improving TiO₂ anatase nanostability via interface segregation: the role of the ionic radius. J Phys Chem C. 2023;127(3):1536–47. https://doi.org/10.1021/acs.jpcc.2c04271
- Caliman LB, da Silva AL, Gouvêa D. Self-segregation and solubility in nonstoichiometric MgAl₂O₄ nanoparticles. J Am Ceram Soc. 2022;105(7):4994–5002. https://doi.org/10.1111/jace. 18440
- Fortes GM, da Silva AL, Caliman LB, Fonseca FC, Gouvêa D. Interfacial segregation in Cl-doped nano-ZnO polycrystalline semiconductors and its effect on electrical properties. Ceram Int. 2021;47(17):24860-67. https://doi.org/10.1016/j.ceramint.2021.05.212
- Gandelman H, da Silva AL, Caliman LB, Gouvêa D. Surface and grain boundary excess of ZnO-doped TiO₂ anatase nanopowders. Ceram Int. 2018;44(10):11390–96. https://doi.org/10.1016/j. ceramint.2018.03.190
- 22. Blaakmeer ES, Rosciano F, Van Eck ERH. Lithium doping of $MgAl_2O_4$ and $ZnAl_2O_4$ investigated by high-resolution solid state NMR. J Phys Chem C. 2015;119(14):7565–77. https://doi.org/10.1021/jp512304e
- 23. Faulkner RA, DiVerdi JA, Yang Y, Kobayashi T, Maciel GE. The surface of nanoparticle silicon as studied by solid-state NMR. Mater. 2013;6(1):18–46. https://doi.org/10.3390/ma6010018
- 24. Marbella LE, Millstone JE. NMR techniques for noble metal nanoparticles. Chem Mater. 2015;27(8):2721–39. https://doi.org/10.1021/cm504809c
- Rees GJ, Orr ST, Barrett LO, Fisher JM, Houghton J, Spikes GH, et al. Characterisation of platinum-based fuel cell catalyst materials using ¹⁹⁵Pt wideline solid state NMR. Phys Chem Chem Phys. 2013;15(40):17195–207. https://doi.org/10.1039/c3cp52268g
- Muche DNF, Drazin JW, Mardinly J, Dey S, Castro RHR. Colossal grain boundary strengthening in ultrafine nanocrystalline oxides. Mater Lett. 2017;186:298–300. https://doi.org/10.1016/j.matlet.2016.10.035
- 27. de Oliveira RAMP, da Silva AL, Caliman LB, Gouvêa D. Interface excess on $\text{Li}_2\text{O-doped}~\gamma\text{-Al}_2\text{O}_3$ nanoparticles. Ceram Int. 2020;46:10555–60. https://doi.org/10.1016/j.ceramint.2020. 01.057

- Han D, Zhang J, Liu P, Li G, Wang S. Densification and microstructure evolution of reactively sintered transparent spinel ceramics. Ceram Int. 2018;44(10):11101–8. https://doi.org/ 10.1016/j.ceramint.2018.03.109
- IIDA Y. Evaporation of lithium oxide from solid solution of lithium oxide in nickel oxide. J Am Ceram Soc. 1960;43(3):171– 72. https://doi.org/10.1111/j.1151-2916.1960.tb14336.x
- Konar B, Van Ende MA, Jung IH. Critical evaluation and thermodynamic optimization of the Li₂O-Al₂O₃ and Li₂O-MgO-Al₂O₃ systems. Metall Mater Trans B. 2018;49(5):2917-44. https://doi.org/10.1007/s11663-018-1349-x
- 31. Rosciano F, Pescarmona PP, Houthoofd K, Persoons A, Bottke P, Wilkening M. Towards a lattice-matching solid-state battery: synthesis of a new class of lithium-ion conductors with the spinel structure. Phys Chem Chem Phys. 2013;15(16):6107–12. https://doi.org/10.1039/c3cp50803j
- MacKenzie KJD, Smith ME. Chapter 1 Introduction. In: Multinuclear solid-state NMR of inorganic materials. Vol. 6. Oxford: Pergamon; 2002. p. 3–19. https://doi.org/10.1016/S1470-1804(02) 80002-5
- Meyer BM, Leifer N, Sakamoto S, Greenbaum SG, Grey CP. High field multinuclear NMR investigation of the SEI layer in lithium rechargeable batteries. Electrochem Solid State Lett. 2005;8(3):145–48. https://doi.org/10.1149/1. 1854117
- 34. Luca V, Hanley TL, Roberts NK, Howe RF. NMR and X-ray absorption study of lithium intercalation in microand nanocrystalline anatase. Chem Mater. 1999;11(8):2089–102. https://doi.org/10.1021/cm990007j
- 35. Wagemaker M, Van de Krol R, Kentgens APM, Van Well AA, Mulder FM. Two phase morphology limits lithium diffusion in TiO₂ (anatase): a ⁷Li MAS NMR study. J Am Chem Soc. 2001;123(46):11454–61. https://doi.org/10.1021/ja0161148
- Hou X, Kirkpatrick RJ. Thermal evolution of the CI⁻-LiAl₂ layered double hydroxide: a multinuclear MAS NMR and XRD perspective. Inorg Chem. 2001;40(25):6397–404. https://doi.org/10.1021/ic010671d
- 37. Stewart FF, Stebbins JF, Peterson ES, Farnan I, Dunham SO, Adams E, et al. Mobility and relaxation determinations of lithium in lithium alumínate ceramics using solid-state NMR spectroscopy. Chem Mater. 1995;7(2):363–67. https://doi.org/10.1021/cm00050a020
- Famery R, Queyroux F, Gilles JC, Herpin P. Etude structurale de la forme ordonnée de LiAl₅O₈. J Solid State Chem. 1979;30(2):257–63. https://doi.org/10.1016/0022-4596(79) 90107-5
- Nuns N, Béclin F, Crampon J. Grain-boundary characterization in a nonstoichiometric fine-grained magnesium aluminate spinel: effects of defect segregation at the space-charge layers. J Am Ceram Soc. 2009;92(4):870–75. https://doi.org/10.1111/j.1551-2916.2008.02901.x
- Chiang Y-M, Kingery WD. Grain-boundary migration in non-stoichiometric solid solutions of magnesium aluminate spinel:
 I. Grain growth studies. J Am Ceram Soc. 1989;72(2):271–77. https://doi.org/10.1111/j.1151-2916.1989.tb06113.x
- Chiang Y-M, Kingery WD. Grain-boundary migration in nonstoichiometric solid solutions of magnesium aluminate spinel:
 II. Effects of grain-boundary nonstoichiometry. J Am Ceram

journal

- 42. Rubat Du Merac M, Reimanis IE, Kleebe HJ. Electrochemical impedance spectroscopy of transparent polycrystalline magnesium aluminate (MgAl₂O₄) spinel. J Am Ceram Soc. 2015;98(7):2130-38. https://doi.org/10.1111/jace.13596
- 43. Munir ZA, Anselmi-Tamburini U, Ohyanagi M. The effect of electric field and pressure on the synthesis and consolidation of materials: a review of the spark plasma sintering method. J Mater Sci. 2006;41(3):763-77. https://doi.org/10.1007/s10853-006-6555-2
- 44. Mordekovitz Y, Shelly L, Halabi M, Kalabukhov S, Hayun S. The effect of lithium doping on the sintering and grain growth of SPS-processed, non-stoichiometric magnesium aluminate spinel. Mater. 2016;9(6):12. https://doi.org/10.3390/ma9060481

SUPPORTING INFORMATION

Additional supporting information can be found online in the Supporting Information section at the end of this article.

How to cite this article: Bernardes AA, da Silva AL, Bettini J, Freitas JCC, Castro RHR, Gouvêa D. Solid-state NMR for the analysis of interface excesses in Li-doped MgAl₂O₄ nanocrystals. J Am Ceram Soc. 2024;107:1334-1347.

https://doi.org/10.1111/jace.19496